Analysis of ligamentary atomization of highly perturbed liquid sheets

Trung-Thanh Vu, Christophe Dumouchel

To cite this version:

Trung-Thanh Vu, Christophe Dumouchel. Analysis of ligamentary atomization of highly perturbed liquid sheets. International Journal of Multiphase Flow, 2018, 107, pp.156-167. ⟨10.1016/j.ijmultiphaseflow.2018.05.027⟩. ⟨hal-01864185⟩

HAL Id: hal-01864185
https://normandie-univ.hal.science/hal-01864185v1

Submitted on 27 Aug 2019

Analysis of Ligamentary Atomization of Highly Perturbed Liquid Sheets

Trung-Thanh Vu, Christophe Dumouchel

CORIA – UMR 6614

Normandie Université, CNRS, Université et INSA de Rouen

Avenue de l'Université, BP 12

76801 Saint-Etienne du Rouvray, FRANCE

Abstract

Ligamentary structures are often encountered in liquid atomization processes. They appear for instance during the atomization of liquid sheets issuing from triple-disk nozzles. Because of the development of turbulence along the internal wall of the discharge orifice, these sheets are highly perturbed and exhibit the formation of ligaments along their sides. The present investigation addresses the question of the origin of size dispersion of the droplets emanating from the atomization of these ligaments. The adopted strategy consists in describing the atomization process reported by experimental images by using a multi-scale tool and in conducting an analysis that concentrates on the dynamic of the small structures carried by the ligaments that might be the main small droplets providers. The advantages of the tool are its ease of application as well as its capacity to bring an information that incorporate the shape of the analyzed interface. The statistical scale analysis demonstrates that the small structures carried by the ligaments are subject to an elongation mechanism whose strength varies from one liquid to another. This mechanism is not dominant in the production of the small drops from the breakup of the ligaments. The dispersion of the drop size distribution, represented by the order of a Gamma distribution, is found to strongly correlate with the initial deformation of the ligaments. An interesting result here is the ease of characterizing the average ligament deformation with the concept of scale distribution. The fact that a single parameter is sufficient to represent the drop size dispersion and that this dispersion correlates with the ligaments deformation suggests the dominance of a single mechanism in the ligament breakup, i.e., the capillary mechanism. As demonstrated in a previous investigation, capillary mechanism is associated with elongation mechanism at small scales. All these results are strengthened by the fact that the explored experimental conditions are uncorrelated.

Keywords: Liquid atomization; Sprays; Multi-scale analysis; Drop size distribution; Liquid ligament

1 Introduction

The breakup of liquid ligaments into a set of droplets has often been identified as the last stage in uncontrolled liquid atomization processes. The production of ligaments may result from the development of a Rayleigh-Taylor instability as reported on a flapping radial liquid sheet (Villermaux and Clanet, 2002) or on an air-assisted cylindrical jet (Marmottant and Villermaux, 2004a). The development of perturbations observed on the borders of a liquid sheet produced by the impact of cylindrical jets always creates ligaments (Brémond and Villermaux, 2006). A highly perturbed liquid sheet shaped by a double contra-rotating swirling flow rearranges as a ligament network before producing the final drops (Dumouchel and Grout, 2009). The mechanism of breakup of liquid ligament is therefore an important point to be addressed.

Villermaux et al. (2004) and Marmottant and Villermaux (2004a) suggested a coalescence type mechanism to represent the fragmentation of a liquid ligament from the instant at which it detaches the bulk flow. This suggestion is motivated by the fact that some of the drops have substantially larger sizes than the ligament itself. The coalescence mechanism establishes that the diameters of the drops are distributed according to a Gamma distribution of order ν:

$$f_0(D) = \frac{\nu^\nu}{\Gamma(\nu)} \frac{D^{\nu-1}}{D_{10}{}^\nu} exp\left(-\nu \frac{D}{D_{10}}\right) \tag{1}$$

where $\Gamma(\nu)$ is the Gamma function. The Gamma distribution has two parameters, i.e., D_{10} and ν. The size parameter, D_{10}, is the arithmetic mean diameter of the distribution (refer to Mugele and Evans (1951) for the mean diameter series definition): it positions the distribution in the diameter space. The order ν is the dispersion parameter: it controls the shape of the distribution. In particular, when D tends towards zero, the distribution becomes $f_0(D) \propto D^{\nu-1}$: a small order designates a high dispersion in the small diameter range. On the other hand, a high order characterizes a set of drops with similar sizes.

The ν-order Gamma distribution was found competent to represent the sizes of the drops produced by the fragmentation of ligaments in several experimental situations (Marmottant and Villermaux, 2004a, 2004b; Brémond and Villermaux, 2006; Tratnig and Brenn, 2010; Dumouchel *et al.*, 2015; Kershavarz *et al.*, 2016). The atomization of ligaments issuing from the Rayleigh-Taylor instability that develops on a cylindrical jet interface surrounded by a high-speed air stream reported order ν ranging from 2 to 4 according to the air velocity (Marmottant and Villermaux, 2004a). Considering the fragmentation of stretched liquid ligaments, Marmottant and Villermaux (2004b) found that the order ν of the drop diameter distribution is actually related to the deformation of the ligament at initial time, i.e., when it detaches from the bulk. This deformation is associated with a series of spherical blobs of diameter δ that allows fitting the initial ligament. It is established that:

$$\nu = \frac{\delta_{10}^2}{\delta_{20}^2 - \delta_{10}^2} \tag{2}$$

where δ_{10} and δ_{20} are the arithmetic and surface mean diameters of the spherical blobs (refer to Mugele and Evans (1951) for the mean diameter series definition).

The investigation of stretched ligaments (Marmottant and Villermaux, 2004b) underlines the random nature of the out-coming droplet size which manifests by different ligament deformations at initial time for identical operating conditions. It also demonstrates that the stretching motion of the ligament during its formation damps the capillary contraction. Stretching therefore influences the detachment event and the subsequent initial deformation.

The influence of the shape of a ligament on its behavior has also been addressed by Tong and Wang (2007). This numerical investigation of moderately elongated ligaments demonstrated that their relaxation dynamic was governed by the initial shape of the ligament and by its Ohnesorge number. In particular the end shape of the ligament is essential in the breakup process.

In a previous work (Dumouchel *et al.*, 2015), ligaments emanating from highly-perturbed liquid sheets was investigated. A multi-scale tool described the ligaments from their detachment from the bulk flow to their subsequent breakup. One of the advantages of this tool is its ability to describe any system with a continuous function – the scale distribution – even if it is constituted of a few droplets. Furthermore, the requirement for these droplets to be spherical is not necessary anymore and the multi-scale tool includes this information in the description it provides. Thanks to this tool, the investigation of individual ligaments was performed. The analysis introduced the notion of equivalent system, i.e., a set of spheres whose scale distribution is the same as the actual system. The equivalent system corresponding to the drops was found to have a diameter distribution well represented by a Gamma distribution. The order ν ranged from 3 to 125 and appeared connected to a Weber number defined as the square of the product of the initial ligament capillary time with its stretching rate. This Weber number was associated with the presence of thin liquid threads between bulges during the ligament deformation. These threads were able to produce small droplets according to a mechanism described by Tong and Wang (2007). However, the connection between this number and the initial deformation of the ligament was not established.

Finally the Gamma distribution was found able to represent the size distribution of droplets issuing from the atomization of an air-assisted jet of polymeric solutions (Kershavarz *et al.*, 2016). That investigation also pointed out the existence of a minimum value for the order ν

($\nu_{min} = 4$) for ligament mediated sprays. Surprisingly, some results in the literature (Marmottant and Villermaux, 2004a, Dumouchel *et al.*, 2015) reported smaller values for the order ν.

The present experimental work considers the ligaments that emanate from highly-perturbed liquid sheets shaped by a double contra-rotating swirling flow. The objective is to identify the origin of the dispersion of the drops they produce. The investigation concentrates on the impact of the initial deformation of the ligaments and of the dynamics of the thin threads they develop while approaching breakup. Contrary to the previous investigation mentioned above (Dumouchel *et al.*, 2015), the ligaments are not individually considered, but a mean behavior is searched. Therefore the randomness of the ligament production and atomization are out of the context of this work. In order to identify representative and general behaviors, it is decided to consider uncorrelated working conditions which are achieved by using several liquids with different physical properties. The analysis of the atomization process and of the spray is based on the multi-scale description of the liquid system. To demonstrate the positive contribution of the multi-scale tool is also an objective of this work.

2 Experimental Setup, Diagnostic and Image Processing

The experimental setup allows feeding an atomizer with a liquid kept in a pressurized tank. This tank is equipped with a piston separating the two phases and avoiding air dissolution in the liquid when the gas is under pressure. The pressurization of the reservoir is controlled by the compressed network of the laboratory. The liquid is filtered and the injection pressure taken as reference is measured just before the atomizer. This latter is mounted on a 3D displacement system and the spray it produces is gently evacuated by an aspirating system.

The atomizer is equipped with a triple-disk nozzle made of the superposition of three circular disks each of them being perforated by a circular orifice (see Fig. 1). The circular hole in disk 3 is the atomizer discharge orifice. As illustrated in Fig. 1, the disks differ by their thickness as well as by the diameter of their orifice. Furthermore, the shift of the discharge orifice-axis, i.e., the eccentricity *e*, is an important geometrical characteristic of the nozzle. As demonstrated in a previous experimental investigation (Dumouchel *et al.*, 2005), the triple-disk nozzle favors the development of a turbulent flow with a double contra-rotating swirl in the discharge orifice which results in the production of a 2D highly-perturbed liquid sheet. This sheet reorganizes as a ligament network which atomizes into droplets of different size. The surface energy per unit volume of the spray correlates with the sum of the non-axial kinetic energy and of the turbulent kinetic energy of the flow issuing from the nozzle (Dumouchel *et al.*, 2005).

Six solutions are used in this work. They are blends of isopropanol with water with a volumetric proportion ranging from 0% (S0) to 10% (S10). The physical properties (surface tension, σ, density, ρ_L, and dynamic viscosity, μ) of these mixtures are gathered in Table 1. They mainly differ by their surface tension and, to a less extent, by their dynamic viscosity. A unique and low value of the injection pressure (0.1 MPa) was selected. This enhances an atomization process with thick structures that are easier to visualize and, therefore, to analyze. For each solution, the mass flow rate is measured by weighting the liquid issuing from the nozzle during a controlled time interval. (A long collecting time is chosen to limit the inaccuracy on the mass flow rate measurement. This inaccuracy is less than 4%.) Dividing this mass flow rate by the solution density and the discharge orifice section area gives the mass flux average velocity named V_q. This velocity, as well as the Reynolds number Re ($= \rho_L V_q D_{ori} / \mu$), the liquid Weber number We ($= \rho_L V_q^2 D_{ori} / \sigma$) and the gaseous Weber number We_G ($= \rho_G V_q^2 D_{ori} / \sigma$ where ρ_G is the air density) characterizing the issuing flow are given in Table 1. The average velocity shows a slight variation with the solution. The Reynolds number decreases with the percentage of isopropanol. For each solution, it indicates that a non-negligible level of turbulence is expected. For all solutions, the gaseous Weber number is never greater than 1. Based on the cylindrical jet theory (Sterling and Sleicher, 1975), these values are low enough to ignore the aerodynamic effects in the atomization process.

A back-light optical arrangement is implemented to image the liquid sheet atomization process from the nozzle exit down to the spray region. The optical axis is perpendicular to the liquid sheet. The light source is a HSPS Nanolite flash lamp which emits an incoherent and wide-spectrum pulse whose duration is 15 ns. A lens is positioned between the lamp and the liquid sheet in order to concentrate the light on the region of interest, i.e., the liquid flow. The detector is a CCD DALSA Panthera 11M4 camera with a definition of 4016 x 2672 pixel^2. The pixel size is 9 µm. The camera is equipped with an objective and an extension ring in order to cover an area of 14.06 x 9.35 mm^2 which corresponds to a spatial resolution equal to 3.5 µm/pixel. In this configuration, the light source plays the role of the shutter. Considering that the flow velocity is of the order of 9 m/s for all solutions (see Table 1), the maximum displacement during the light flash is 0.135 µm which is far less than the spatial resolution. Therefore, we expect the image to be free of any blurred. The half-height width of the PSF (Point Spread Function) is determined according to Fdida and Blaisot (2010) and is found equal to 28 µm. The MTF (Modulation Transfer Function) of the optical setup is equal to the amplitude of PSF Fourier transform. Assuming a Gaussian PSF allows evaluating the MTF as well as the corresponding cut-off spatial frequency that is equal to 0.15 µm^{-1}. These figures indicate that the detection of details of the order of 28 µm may be altered by the optical system and that elements smaller than 7 µm cannot appear on the image. Finally, considering a previous article using the same equipment (Dumouchel and Blaisot, 2014), we know that the depth of field of the optical setup is not limiting since the atomization process and spray are planar, and this is particularly the case in the near nozzle field where the study concentrates.

In order to cover the whole atomization process, two series of images are taken. For the first series (top views), the exit plane of the atomizer appears on the top of the image and the exploitable field of observation covers the positions $z = 0$ (atomizer position) to $z = 7$ mm. For the second (bottom views), the atomizer has been shifted 3.5 mm up and the exploitable field of observation covers the position $z = 3.5$ mm to $z = 10.5$ mm. For each atomizer position and for each solution, 150 images are taken in order to perform a statistical analysis.

A typical top view image is presented in Fig. 2 for every solution. These images show alike atomization process. As soon as the liquid flow issues from the orifice, it extends to produce a liquid sheet whose borders are perturbed. Further downstream, two mechanisms coexist: the open and contraction of the sheet and the development of lateral ligaments. These images underline a strong influence of the liquid. Noticeable differences concern both the behavior of the sheet whose expansion and contraction are more or less pronounced and the ligaments whose size, number, regularity, position, behavior and fragmentation vary significantly. These differences result from important modification of the internal nozzle flow since, as reminded above, the atomization process of the liquid flow produced by triple-nozzle depends on the non-axial kinetic energy and the turbulent kinetic energy of the issuing flow. The important differences observed on the images show that the six situations are not comparable and that they should be considered as individual cases. Some results presented later will confirm this point.

The images are treated in order to provide two-level images where the liquid appears as black pixels on a white background. The first step of the image processing is the normalization aiming to correct the background inhomogeneity as well as image-to-image variations. The second step is the localization in order to find the position of the liquid gas interface. For this specific purpose, two methods are used. The first method is a single-threshold method that is convenient to identify the large liquid structure such as the liquid sheet, the ligaments and the big droplets. The appropriate threshold for this first method is determined from the gray level histograms of the normalized images. The drawback of the single threshold method is its propensity to ignore the small elements that are not in focus and therefore whose contrast is too weak to be seen. For such elements, a second method based on the wavelet-transformation technique is necessary. This technique, fully detailed in Fdida and Blaisot (2010), is particularly well appropriate in the present case for the detection of the smallest droplets.

3 Multi-scale description: introduction and measurements

The concept of 2D multi-scale description and analysis of free liquid flows has been introduced in several previous articles (Dumouchel and Grout, 2009, Dumouchel *et al.*, 2015, 2017 for instance). The 2D multi-scale description of a liquid system consists in measuring the cumulative scale distribution $E_2(d)$ on its 2D projection reported by an image. Inspired from the Euclidean Distance Mapping method to measure fractal dimension (Bérubé and Jébrac, 1999), the cumulative scale distribution is built from successive erosion operations for a scale d ranging from 0 to infinity. The erosion operation at scale d consists in removing a strip of width $d/2$ around the whole system. The cumulative scale distribution $E_2(d)$ is the measurement of the relative amount of system surface area that is removed by the erosion operation at scale d. If S_T designates the total surface area of the system 2D projection and if $S(d)$ stands for the remaining surface area after the erosion operation at scale d, $E_2(d)$ writes:

$$E_2(d) = \frac{S_T - S(d)}{S_T} \tag{3}$$

For $d = 0$, $S(d) = S_T$ and $E_2(0) = 0$. For a sufficiently large scale, the erosion operation removes all the system: the remaining surface area $S(d) = 0$ and $E_2(d) = 1$. For intermediate scales, $S(d)$ keeps decreasing while d increases. Therefore, $E_2(d)$ is a cumulative function and the smallest scale for which $E_2(d) = 1$ is the maximum scale d_{max}.

The first derivative of $E_2(d)$ in the space scale introduces the scale distribution $e_2(d)$:

$$e_2(d)=\frac{\mathrm{d}E_2(d)}{\mathrm{d}d}=\frac{P(d)}{2S_T} \tag{4}$$

As indicated by this equation, the scale distribution $e_2(d)$ is the ratio of the perimeter $P(d)$ of the eroded system at scale d on twice the surface-area S_T. The dimension of $e_2(d)$ is the inverse of a length. The distributions $E_2(d)$, $e_2(d)$ and $P(d)$ depend on the shape of the system but they are not a measurement of this shape since systems with different shapes may report identical scale distributions. When the liquid system deforms, the above functions become time dependent and allow investigating the dynamic of the deformation process at selected scales.

Since the behavior of liquid ligaments is the main topic of the present investigation, let us consider the case of a smooth and cylindrical ligament. The 2D projection of this system is a rectangle whose width is equal to the diameter D_L of the ligament. By considering the lateral surface of the ligament only, it is easy to demonstrate that its scale distribution is given by:

$$\begin{cases} e_2(d)=\dfrac{1}{D_L} & d<D_L \\ e_2(d)=0 & d\geq D_L \end{cases} \tag{5}$$

The scale distribution is independent of the scale d. This characteristic results from the absence of geometrical deformation of the cylindrical ligament. In other word, a deformed ligament will report a scale-dependent distribution and this scale dependence will be a characteristic of the deformation.

Keeping its smooth and cylindrical shape, the ligament is supposed to evolve with time, i.e., its scale distribution and/or perimeter distribution are both time dependent. Combining the quasi one-dimensional continuity equation provided by Stelter et al. (2000) together with the fact that the section of the ligament is constant along the axial direction z, the rate of stretching T associated to the diameter evolution is:

$$T(t)=\frac{\partial v}{\partial z}=\frac{-2}{D(t)}\frac{\mathrm{d}D(t)}{\mathrm{d}t} \tag{6}$$

where v designates the longitudinal velocity. Considering Eq. (5), the rate of stretching can be expressed as a function of the scale distribution $e_2(d,t)$:

$$T(t)=T_e(d,t)=2\frac{\dot{e}_2(d,t)}{e_2(d,t)} \tag{7}$$

where the dot indicates a temporal derivative. Furthermore, the variation rate $T_P(d,t)$ of the perimeter can be introduced also:

$$T_P(d,t)=\frac{\dot{P}(d,t)}{P(d,t)} \tag{8}$$

The comparison between the variation rates given Eqs. (7) and (8) allows identifying three possible mechanisms responsible for the ligament evolution.

1 – The Elongation Mechanism (EM): The ligament is elongated by an external constraint and its volume is constant. The relationship between $D(t)$ and $P(0,t)$ imposed by the volume conservation allows demonstrating that this mechanism is characterized by $T_e(d,t) = T_P(d,t)$.

2 – The Contraction Mechanism (CM): The ligament contracts under a driving force that expulses the liquid out of the ligament. This is observed for instance on liquid bridges submitted

to capillary contraction mechanism. In this situation the volume of the ligament is not constant anymore and since its length doesn't vary, it is characterized by $T_P(d,t) = 0$.

3 – The Lengthening Mechanism (LM): The ligament is created and reports an increasing perimeter but a constant diameter. Such a mechanism is characterized by $T_e(d,t) = 0$.

From a more general point of view, the variation rates $T_P(d,t)$ and $T_e(d,t)$ give information on two different dynamics: $T_P(d,t)$ characterizes the dynamic of the perimeter of the system eroded at scale d and $T_e(d,t)$ characterizes the dynamic of the temporal deformation (variation of the shape during time) of the system eroded at scale d. The dependence of these variation rates with the scale d is a mark of geometrical deformation (variation of shape in the scale space) of the system. For the three mechanisms introduced above, there is no geometrical deformation (the derivative in the scale space $e_2'(d,t) = 0$) since the cylindrical system remains smooth, and there is no temporal deformation ($T_e(d,t) = 0$) for LM since for all scales the amount of length per unit surface remains unvaried for this mechanism.

The advantage of the scale distribution is its ease of measurements and the possibility it offers to treat and consider any system whatever its deformation. In the present work the scale distribution is measured for the whole system in order to describe the liquid atomization process and for the drops produced by the ligaments. These measurements are performed with the two-level images introduced in Section 2.

The temporal description of the atomization process is obtained by performing the measurement on a portion of the liquid system that is delimited by a rectangular analyzing window and by shifting this window from the top to the bottom of the image. The position h of the analyzing window is converted into an equivalent time $t = h/V_q$. For each liquid, this treatment is performed on the 150 images with the software ImageJ and the mean cumulative scale distribution $E_2(d,t)$ is obtained. The height h_w = 100 pixels of the analyzing window was selected according to a procedure described in a previous work (Dumouchel and Grout, 2009). The shift of the analyzing window was fixed at 100 pixels. This corresponds to a temporal resolution of the order of 0.04 ms for every solution. The scale distribution $e_2(d,t)$, first derivative in the scale space of the cumulative distribution $E_2(d,t)$ (Eq. (4)), is calculated. The behavior of $e_2(d,t)$ for $d \in [0; 35\ \mu m]$ was non-physical. (This scale interval corresponds to the five first erosion operations.) The main reason for this problem is the pixelization and the impossibility to accurately describe a smooth contour with a square grid. To get rid of this drawback, the linear behavior always observed for the scale range $d \in [40\ \mu m; 100\ \mu m]$ was extended down to the scale $d = 0$. Implicitly, this procedure removes from the analysis all details with a characteristic length than 40 μm. We note here that the limitation imposed by the pixelization is more severe than the one imposed by the optical setup since its half-height width PSF is 28 μm. However, thanks to the use of a low injection pressure, this limitation is not too pejorative since details less than 40 are not numerous and not majority as evidenced by the results presented in the next section.

The characterization of the drops produced by the ligaments is conducted in two steps: 1 – identification of the drops, 2 – measurements of the scale distribution of these drops. The first step consists in extracting all detached fragments on the top-view and bottom-view images and to attribute to each of them an equivalent diameter defined as the diameter of the circle that has the same surface area as the detached fragment. Then, the volume-based distribution of these equivalent diameters is built. For the solution S0 this distribution is displayed in Fig. 3. It shows two main peaks (at 250 μm and 900 μm) highlighting two different populations. We assume that the left peak designates the population of drops produced by the ligaments whereas the right peak corresponds to bigger fragments such as detached ligaments whose atomization is not complete. These two peaks are distinguishable enough to identify a maximum diameter of the drops produced by the ligaments. In Fig. 3 this maximum diameter is of the order of 600 µm. It is of the same order for the five other cases.

The second step consists in measuring the scale distribution of the system composed of all these drops. As for the global liquid system, this measurement goes through the determination of the cumulative distribution $E_2(d)$ and to the calculation of its derivative $e_2(d)$. Here again, the distribution $e_2(d)$ revealed unphysical behavior in the first scales and required to be adjusted. The procedure was similar to the one applied for the complete system scale distribution: the dependence for scales ranging from 40 µm to 100 µm was extended down to $d = 0$. This time, this dependence was polynomial. Thus, droplets less than 40 µm were not included in the scale distribution measurement. Considering the equivalent diameter range (Fig. 3) the impact of this limitation is believed to be weak.

4 Results and analysis

Figure 4 shows the temporal evolution of the scale distribution $e_2(d,t)$ for the solutions S0 and S10 (Fig. 4a and 4b, respectively). First, we note that the scale interval covered by the distribution is far much larger than the limitation due to pixelization. Second, we note that, for both solutions, the evolution looks alike. At the initial time ($t = 0.10$ ms), the scale distribution is rather constant up to $d = 750$ µm as if the system was perceived as a rectangle (see Eq. (5)). This denotes an absence of small scale perturbations. Then, the scale distribution smoothly decreases between $d = 750$ µm and 1000 µm, which results from the triangular shape of the sheet as well as possible large scale perturbations.

As time increases, a peak develops at $d = 0$ ($e_2(0,t)$ increases) due to the development of the ligaments and a more or less inclined linear behavior spreads in the large scale region due to the contribution of the liquid sheet (d_{max} increases and then decreases). The increase of $e_2(0,t)$ attests the creation of liquid-gas interface during the process. The variation of d_{max} represents the creation and contraction of the liquid sheet. The evolution of these two characteristics differs between solutions S0 and S10. The maximum scale d_{max} reaches higher values for S10 and the final value of $e_2(0,t)$ is also higher for S10. These two observations correlate with each other since higher d_{max} denote thinner liquid sheets and therefore the production of thinner ligaments and subsequently of smaller drops. Thus, the final spray presents a higher amount of interface per unit volume as suggested by the higher $e_2(0,t)$.

The scale d_{max} is determined from the cumulative distribution $E_2(d,t)$ as the smallest scale for which $E_2(d,t) > 0.99$. The results are presented in Fig. 5 for all solutions under a non-dimensional form that has been inspired by Bremond and Villermaux's investigation (2006) on the behavior of liquid sheets produced by the impact of two cylindrical jets. When the Reynolds number of these jets is lower than 2400, a smooth stable and contracting sheet is produced. The contraction mechanism results from a competition between the surface tension force and the centrifugal force that apply on the rim of the sheet. For a fixed impact angle, it is demonstrated that the shape of the sheet is constant in the space (x/D_jWe; y/D_jWe) where x and y are the width and height Cartesian coordinates respectively, D_j is the diameter of the jets and We is the jet liquid Weber number. In Fig. 5, d_{max} replaces the coordinate x, D_{ori} replaces D_j, V_qt is taken as the coordinate y, and We is the liquid Weber number (Table 1). As noted above, the creation of the sheet right at the nozzle exit and its subsequent contraction further downstream are reproduced by an increase and a decrease of d_{max}. The maximum of d_{max} for liquid S0, S1, S2 and S5 appear roughly at the same location in agreement with the model of Brémond and Villermaux (2006). Noting that the sheet angles are close one to another (between 33° and 41°) this suggests that for these four solutions, the development of the perturbation along the sheet has a limited influence on the sheet contraction mechanism that occurs as in the absence of perturbation. This is not the case for solutions S3 and S10 for which the maximum of d_{max} appears earlier and reports a lower value. For these two solutions, it is suspected that the development of the perturbations on the sheet border induces a premature contraction of the sheet as observed by Bremond and Villermaux (2006) in the case of high initial perturbation amplitudes. Note also that the decrease of d_{max} after the maximum is rather linear and parallel for the solutions S1, S2, S5 and S10. This behavior suggests that the limit sheet contraction mechanism identified by Bremond and Villermaux (2006) is reached. This mechanism occurs in the absence of rim, i.e., when no rim centrifugal inertia effect participates to the sheet contraction that becomes controlled by the surface tension forces only. The solutions S0 and S3 have not reached this extreme behavior and report a slower contraction dynamics. The results provided by the examination of the scale d_{max} confirm that the six operating conditions cover different physical scenarios and therefore must be seen as individual situations.

For every solution Fig. 6 presents the temporal evolution of the variation rates $T_e(0,t)$ and $T_P(0,t)$ introduced by Eq. (7) and (8), respectively. The variation rate $T_P(0,t)$ is always positive and continuously decrease with time indicating a continuous perimeter production but with a decreasing efficiency. $T_P(0,t)$ reaches zero for a time of the order of 1-1.2 ms according to the solution. This time corresponds to the end of the atomization process in term of interface production as it is detected on the images. These behaviors indicate that the main mechanism responsible for the interface production is the reorganization of the system as ligaments. This mechanism is dominant in the first half of the atomization process. The breakup of these ligaments dominates the second half of the atomization process and is globally less efficient in term of interface production.

The temporal evolution of $T_e(0,t)$ gives information on the temporal deformation of the whole system ($d = 0$). This evolution is similar for all solutions. At the initial time, $T_e(0,t)$ is close to zero. Then it increases to reach a plateau. Finally, it increases up to a maximum before continuously decreasing until the end of the atomization process. For solution S0, the maximum before the final decreases is not observed. The initial value $T_e(0,t) = 0$ indicates a weak development of small scale perturbations at the beginning of the process. The increase of $T_e(0,t)$ and the subsequent plateau cover the liquid sheet expansion/contraction periods during which the lateral ligaments develop. The production of the ligaments is the dominant mechanism in the temporal deformation of the whole system. The maximum of $T_e(0,t)$ observed for solutions S1 to S10 corresponds to the disappearance of the sheet which occurs fairly suddenly for these solutions. The final decrease of $T_e(0,t)$ characterizes the temporal deformation of the ligaments as they evolve towards breakup. This deformation concerns smaller and smaller and less and less structures as time goes.

The ligaments carry small structures such as thin liquid threads between bulges whose dynamics during the atomization process may significantly influence the size distribution of the small drops produced by these ligaments. This point is addressed in the following. First, we assume that the smallest structures carried by the ligaments are also those carried by the whole system. Second, an average characteristic scale $d_L(t)$ of these structures is identified with the distribution $P(d,t)$. In the small scale region, the $P(d,t)$ distribution always shows a sharp decrease that corresponds to the loss of all small cylindrical structures after the erosion operation performed at their characteristic size. The inflexion point associated with this decrease is believed to occur at the characteristic scale $d_L(t)$ of the smallest structures:

$$\left.\frac{\partial^2 P(d,t)}{\partial d^2}\right|_{d_L} = 0 \qquad (8)$$

The average perimeter $P_L(t)$ delimited by these structures can be approximated by:

$$P_L(t) = P(0,t) - P(d_L,t) \qquad (9)$$

Furthermore, the surface area removed from the whole system by the erosion operation at scale d_L is equal to $S_T(t)E_2(d_L,t)$. It is also the sum of the surface area $S_L(t)$ of the small structures and the surface area removed from the structures whose characteristic scale is higher than d_L. This latter surface can be estimated as $P(d_L,t)d_L/2$. Therefore the surface area $S_L(t)$ can be estimated by:

$$S_L(t) = S_T(t)E_2(d_L,t) - \frac{P(d_L,t)d_L}{2} \tag{10}$$

Note that by introducing Eq. (9) in Eq. (10), $S_L(t)$ becomes:

$$S_L(t) = \frac{P_L(t)d_L}{2} + \left[S_T(t)E_2(d_L,t) - \frac{P(0,t)d_L}{2}\right] \tag{11}$$

The term in bracket is negative. It is a correction of the surface area $P_L(t)d_L/2$ because of the possible geometrical deformation of the small structures whose scale is less than d_L. If this deformation does not exist, the small structures are smooth ligaments and the correcting factor is equal to zero. Finally, the scale distribution $e_{2L}(d,t)$ of the small structures can be calculated for $d = 0$ with Eqs. (4), (9) and (10) since:

$$e_{2L}(0,t) = \frac{P_L(t)}{2S_L(t)} \tag{12}$$

The variation rates characterizing the dynamics of the small structures are therefore given by (see Eqs. (7) and (8)):

$$T_{eL}(t)=2\frac{\dot{e}_{2L}(0,t)}{e_{2L}(0,t)} \qquad T_{PL}(t)=\frac{\dot{P}_L(t)}{P_L(t)} \tag{13}$$

Figure 7 shows the temporal evolution of these two variation rates for every solution. Three time periods can be identified from the evolution of T_{PL}: 1 – increase from 0 to a maximum; 2 – continuous decrease down to zero; 3 – negative values with a sharp peak. At the beginning the small structures are carried by small perturbations from which the lateral ligaments develop. Therefore, during the first time period, the small structures investigated by this analysis are likely the ligaments themselves. Their development is characterized by a fast increase of $T_{PL}(t)$ whereas $T_{eL}(t)$ remains close to zero. This last characteristic corresponds to the lengthening mechanism (LM) introduced in Section 3 and demonstrates that the ligaments are formed by the contraction of the liquid sheet and not by the expulsion of liquid out of the sheet. During the second time period, the ligament formation continues and their deformation starts: the variation rates plotted in Fig. 7 characterize the small structures carried by the ligaments. The perimeter of the small structures still increases with time which seems reasonable since these structures are expected more and more numerous as the breakup is approached. The temporal deformation of these structures is given by the variation rate $T_{eL}(t)$ and appears more or less pronounced according to the time and to the solution. A comparison of the solutions is suggested at the time t^* at which a maximum of $T_{eL}(t)$ is detected (see Fig. 7). Since it appears for every solution, this maximum is likely a characteristic of the atomization process and comparing the solution behavior at this time is meaning full. Figure 8 positions each solution in the ($T_{eL}(t)$; $T_{PL}(t)$) map at $t = t^*$. The basic mechanisms introduced in Section 3 are indicated in the map. We see that the increase in the small structure length revealed by the positive $T_{PL}(t^*)$ is associated with different dynamics according to the solution. The dominating mechanism is the lengthening mechanism for S0 and the elongation mechanism for S10. The four other solutions are between these two mechanisms. We see in Fig. 7 that solutions S1 and S10 display a secondary maximum for $T_{PL}(t)$ associated with a negative peak for $T_{eL}(t)$ during the second period. This behavior is rather similar to what is observed during the first period and correspond to the creation of small structures due to the development of ligaments on the left side of the liquid sheet (see Fig. 2). During the third period, a strong temporal deformation of the small structures occurs ($T_{eL}(t)$ shows a sharp peak) as well as a strong reduction of the perimeter ($T_{PL}(t) < 0$). This corresponds to the fast contraction of the small structures associated with the breakup event of the ligaments. After this last period, both $T_{eL}(t)$ and $T_{PL}(t)$ are equal to zero. This can be seen in Fig. 7 for S3 and S10.

The scale distribution of the drops produced by the ligaments has been measured according to the protocol described in Section 3. The results are presented in Fig. 9 where the distributions appear to extend far beyond the limit scale imposed by the pixelization. Although the distributions look alike, we note that $e_2(0)$ varies from one solution to another denoting a different atomization efficiency. This is more obvious from a mathematical description of these distributions that is achieved by applying the notion of equivalent system mentioned in the introduction (Dumouchel *et al.*, 2015): the system of droplets is represented by a set of spheres whose diameters are distributed according to a Gamma distribution (Eq. (1)) and whose scale distribution is the same as the one of the actual droplet system. It can be demonstrated that the scale distribution of the equivalent system writes:

$$e_2(d) = \frac{2\nu}{D_{10}} \frac{\Gamma\left(\nu+1, \frac{\nu d}{D_{10}}\right) - \frac{\nu d}{D_{10}} \Gamma\left(\nu, \frac{\nu d}{D_{10}}\right)}{\Gamma(\nu+2)} \tag{14}$$

where $\Gamma(x,y)$ represents the incomplete Gamma function. The couples of parameters (ν; D_{10}) that offers the best fit between the measured and the mathematical scale distribution are determined thanks to a Scilab routine written for this purpose. The parameters are listed in Table 1 and the mathematical distributions are plotted in Fig. 9. The agreement is acceptable for all solutions. The order ν of the Gamma distribution is found to range between 2.5 and 4.7. The smallest value is found for S10 and the highest for S0. As noticed in Fig. 8, the temporal deformation of the small structures for F10 is mainly due to an elongation mechanism. This mechanism is expected to promote the production of small droplets (Marmottant and Villermaux, 2004b; Dumouchel *et al.*, 2015). The weight of the elongation mechanism in the temporal deformation of the small structure can be characterized by the ratio $T_{eL}(t)/T_{PL}(t)$: elongation dominates when this ratio is close to 1 (see Fig.8). Figure 10 compares this ratio at $t = t^*$ with the order ν given in Table 1. Globally speaking, we see a degree of correlation between the weight of the elongation mechanism in the small structure dynamic and the order ν which corresponds to the expected one, i.e., the production of small droplets (small ν) is enhanced when the weight of the elongation mechanism increases. However, the scatter of the middle points says that the dynamics of the small structures is not the dominant mechanism controlling the drop diameter dispersion.

To better understand the behavior of the small structures, we introduce the capillary time $t_{\sigma L}(t^*)$ that characterizes them. It is defined by:

$$t_{\sigma L}(t^*) = \sqrt{\frac{\rho}{\sigma e_{2L}^3(t^*)}} \tag{15}$$

Figure 11 presents the ratio $T_{eL}(t^*)/T_{PL}(t^*)$ versus the product $T_{eL}(t^*)t_{\sigma L}(t^*)$. This product compares the characteristic time of the temporal deformation with the characteristic capillary of the small structures. It is equal to the square root of the Weber number introduced in Dumouchel *et al.* (2015) and mentioned in the introduction. Figure 11 shows two points. First, the characteristic capillary time is always smaller than the deformation characteristic time. Second, the three mechanisms represented by $T_{eL}(t^*)$, $T_{PL}(t^*)$ and $t_{\sigma L}(t^*)$ are connected with each other. Therefore, the dynamics of the small structures is controlled by capillary efforts and a part of the elongation mechanism identified on the small structures is likely a consequence of this capillary mechanism. Indeed, it has been demonstrated that a cylindrical ligament submitted to a capillary instability show an elongation process at small scales during the linear growth of the instability (Dumouchel *et al.*, 2017).

The previous result suggests therefore that the ligament deformation and breakup is mainly controlled by capillarity. In consequence, the size of the drops should correlate with the initial shape of the ligaments in a way similar to a capillary instability of a cylindrical jet for which the droplet size can be estimated from the initial perturbation that deforms the jet. In other words, this direct connection would indicate the dominance of one mechanism on the ligament behavior, i.e., the capillarity. An information on the deformation of the ligaments can be suggested from the scale distribution. As mentioned above, the scale distribution contains an information on the shape of the system it describes. Equation (5) says that a smooth ligament has a scale distribution independent of the scale. Thus, a scale dependence is a mark of a geometrical deformation. Therefore, the first derivative of the scale distribution in the scale space for $d = 0$, i.e., $e_2'(0,t)$ should be connected to the geometrical deformation of a ligament. Furthermore, considering that for a smooth ligament ($e_2'(0,t) = 0$) the expected order ν tends to infinity (production of droplets of same diameter), the shape parameter S_P appropriate to describe the geometrical deformation of the ligaments should be inversely proportional to $e_2'(0,t)$. In order to have a non-dimensional parameter, we suggest defining S_P as:

$$S_P = \frac{e_2(0,t)^2}{e_2'(0,t)} \tag{16}$$

S_P is determined for $t = t^*$. We must first make sure that, at this time, the derivative $e_2'(0,t^*)$ is well representative of the ligament deformation and does not contain any information on the sheet deformation. The scale distributions at this time are shown in Fig. 12. They confirm this point. Indeed, for every solution, the scale distribution is rather scale independent in the medium scale range. At t^*, the system is similar to a large rectangle that carries small deformed ligaments. The first derivative $e_2'(0,t^*)$ is clearly a characteristic of the ligaments.

Figure 13 compares the order ν with the shape parameter S_P calculated at t^*. This graph reports a strong correlation fitted by the equation:

$$\nu = 5.34\left(1 - exp\left(-0.91\frac{e_2(0,t^*)^2}{e_2'(0,t^*)}\right)\right) \tag{17}$$

This result says that the dispersion of the size of the droplets produced by ligaments correlates with the initial deformation of these ligaments. This confirms the dominance of the capillary effects in the ligament deformation and breakup. Considering the conclusions due to Marmottant and Villermaux (2004b) and Keshavarz et al. (2016), this result also suggests that the time t^* corresponds to the average time at which the ligaments detach from the bulk. This is more or less confirmed by the images.

5 Conclusions

The evolution of ligaments that develop during the atomization of high perturbed liquid sheets is analyzed. Six cases are considered. The evolution of a characteristic scale of the large structure, i.e., the sheet, evidenced important differences between the experimental situations. The contraction of the liquid sheet appears more or less dependent on the ligament development according to the situation. This point demonstrates that the operating conditions correspond to individual situations which nevertheless show similar atomization process, i.e., the reorganization of a liquid sheet as a ligament network whose subsequent atomization produces the spray. The multi-scale description is filtered at a scale that is representative of the smallest structures present in the process. These structures are liquid threads whose erosion produces a sharp decrease of the amount of interface. Their dynamics is specifically identified and analyzed. It is found that they are subjected to an elongation mechanism whose strength depends on the situation. Although this mechanism impacts the size distribution of the drops emanating from the ligament breakup, its contribution to the distribution dispersion is not dominant. Similarly to previous investigations of the literature, the dispersion of the size distribution is found to correlate with the initial deformation of the ligament. (This deformation is characterized in averaged in the present analysis.) This strong correlation results from the dominance of the capillary efforts in the ligament breakup mechanism. This probably explains why the dispersion of the distribution requires one parameter only to be described, i.e., the order of the Gamma distribution. Furthermore, the elongation mechanism identified on the small scale structures is believed to be similar to those that manifest in a capillary instability developing on an initially smooth liquid jet as identified in a previous investigation. The strength of all these results is increased by the fact that the experimental situations examined here are individual situations.

This analysis highlights the interesting and multiple capacities of the multi-scale description. All results and conclusions are obtained from a single measurement: the one of the cumulative scale distribution. The multi-scale tool can treat any kind of system. For instance no spherical droplets can be treated without losing information on the deviation from sphericity. It is shown here that the multi-scale tool allows treating the question of average deformation of a structure category of an atomization process.

Acknowledgements

This research is conducted as part of the project named MEXCARBU and supported by Direction Générale des Entreprises.

Nomenclature

d	Scale
D	Diameter
e_2	Scale distribution
E_2	Cumulative scale distribution
f_0	Number-based diameter distribution
$P(d)$	Perimeter of the system eroded at scale d
Re	Reynolds number
S_T	System total surface area
$S(d)$	Surface area of system eroded at scale d
T	variation rate
V_q	Average flow velocity
We	Weber number
δ	Blob diameter
Γ	Gamma function
μ	Liquid viscosity
ν	Order of the Gamma distribution
ρ	Density
σ	Surface tension

References

Bérubé, J., Jébrak, M., (1999) High precision boundary fractal analysis for shape characterization. Comput. Geosci. 25, 1059–1071

Brémond, N., Villermaux, E., (2006) Atomization by jet impact. JFM, 549, 273-306

Dumouchel, C., Aniszewski, W., Vu, T.T., Ménard, T., (2017) Multi-scale analysis of simulated capillary instability. IJMF 92, 181-192

Dumouchel, C., Blaisot, J.B., (2014) Laser-diffraction measurement of nonspherical drop sprays. Atomization and Sprays 24, 223-249

Dumouchel, C., Blaisot, J.B., Bouche, E., Ménard, T., Vu, T.T., (2015) Multi-scale analysis of atomizing liquid ligaments. IJMF 73, 251-263

Dumouchel, C., Cousin, J., Triballier, K., (2005) On the role of the liquid flow characteristics on low-Weber number atomization processes. EiF 38, 637–647

Dumouchel, C., Grout, S., (2009) Application of the scale entropy diffusion model to describe a liquid atomization process. IJMF, 35, 952-962

Fdida, N., Blaisot J.B., (2010) Drop size distribution measured by imaging: determination of the measurement by the calibration of the point spread function. Meas. Sci. Technol. 21, n°2, 025501

Keshavarz, B., Houze, E.C., Moore, J.R., Koerner, M.R., McKinley, G.H., (2016) Ligament mediated fragmentation of viscoelastic liquids. PRL, 117, 154502

Marmottant, P., Villermaux, E., (2004a) On spray formation. JFM, 498, 77-111

Marmottant, P., Villermaux, E., (2004b) Fragmentation of stretched liquid ligaments. POF 16, n°8, 2732-2741

Mugele, R.A., Evans, H.D., (1951) Droplet size distribution in sprays. Ind. Engng. Chem. 43, 1317-1324

Stelter, M., Brenn, G., Yarin, A.L., Singh, R.P. and Durst, F., (2000) Validation and Application of a Novel Elongation Device for Polymer Solutions. Journal of Rheology 44, 595-616

Sterling A.M., Sleicher C.A., (1975) The instability of capillary jets. JFM 68, part 3, 477-495

Tong, A.Y., Wang, Z., (2007) Relaxation dynamics of a free elongated liquid ligament. POF 19, 092101

Tratnig, A., Brenn, G., (2010) Drop size spectra in sprays produced from pressure swirl atomizer. IJMF, 36, 349-363

Villermaux, E., Clanet, C., (2002) Life of a flapping liquid sheet. JFM 462, 341-363

Villermaux, E., Marmottant, P., Duplat J., (2004) Ligament-mediated spray formation. PRL, 92, n°7, 074501

Table and Figure Captions

Table 1: Physical properties of the six solutions, mass flux average velocity V_q, Reynolds number Re, liquid Weber number We and gaseous Weber number We_G. Parameters D_{10} and ν of the Gamma distribution.

Figure 1: Top and side views of the triple-disk nozzle

Figure 2: Top view images of the liquid atomization process (from left to right and top to bottom: S0, S1, S2, S3, S5, S10)

Figure 3: Volume-based distribution of the equivalent diameter of the detached liquid fragments for solution S0

Figure 4: Temporal evolution of the scale distribution $e_2(d,t)$. 4a – Solution S0; 4b – Solution S10

Figure 5: Temporal evolution of the maximum scale d_{max}. (The non-dimension is inspired by Brémond and Villermaux, 2006)

Figure 6: Temporal evolution of the variation rates $T_P(0,t)$ and $T_e(0,t)$ (all solutions)

Figure 7: Temporal evolution of the variation rates $T_{PL}(t)$ and $T_{eL}(t)$ (all solutions)

Figure 8: Behavior of the small structures for all solutions at t^* (dash lines represent the basic mechanisms introduced in section 3; LM: Lengthening Mechanism, CM: Contraction Mechanism; EM: Elongation Mechanism)

Figure 9: Measured scale distributions of the drops produced by the ligaments. Mathematical fit with a Gamma distribution (all solutions)

Figure 10: Comparison of the order ν of the gamma distribution with the ratio $T_{eL}(t^*)/T_{PL}(t^*)$

Figure 11: Comparison of $T_{eL}(t^*)/T_{PL}(t^*)$ with $T_{eL}(t^*)t_{\sigma L}(t^*)$

Figure 12: Scale distribution of the whole system for every solution at $t = t^*$

Figure 13: Comparison of the order ν of the gamma distribution with the shape parameter $S_P = e_2(0,t^*)^2/e_2'(0,t^*)$

Table 1

Solution	σ (mN/m)	ρ_L (kg/m^3)	μ (kg/(ms))	V_q (m/s)	Re (-)	We (-)	We_G (-)	D_{10} (µm)	ν (-)
S0	69.3	997.9	$0.99\ 10^{-3}$	8.96	3613	462	0.56	133	4.62
S1	59.1	996.0	$1.03\ 10^{-3}$	8.81	3408	523	0.63	104	3.42
S2	53.7	994.1	$1.07\ 10^{-3}$	8.82	3278	576	0.70	100	3.27
S3	50.5	992.1	$1.14\ 10^{-3}$	9.03	3143	641	0.78	110	3.56
S5	46.2	988.9	$1.26\ 10^{-3}$	9.04	2838	699	0.85	92	2.93
S10	39.8	982.0	$1.62\ 10^{-3}$	9.14	2216	825	1.01	88	2.49

Figure 1

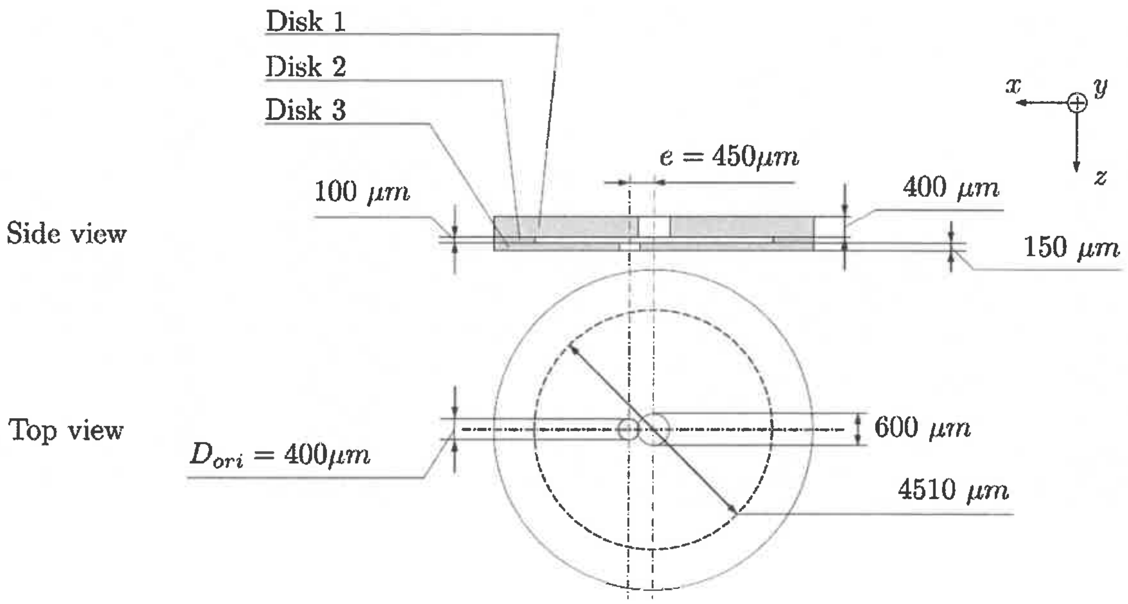
Disk 1
Disk 2
Disk 3
$e = 450\mu m$
x
y
z
$100\ \mu m$
$400\ \mu m$
Side view
$150\ \mu m$
Top view
$600\ \mu m$
$D_{ori} = 400\mu m$
$4510\ \mu m$

Figure 2

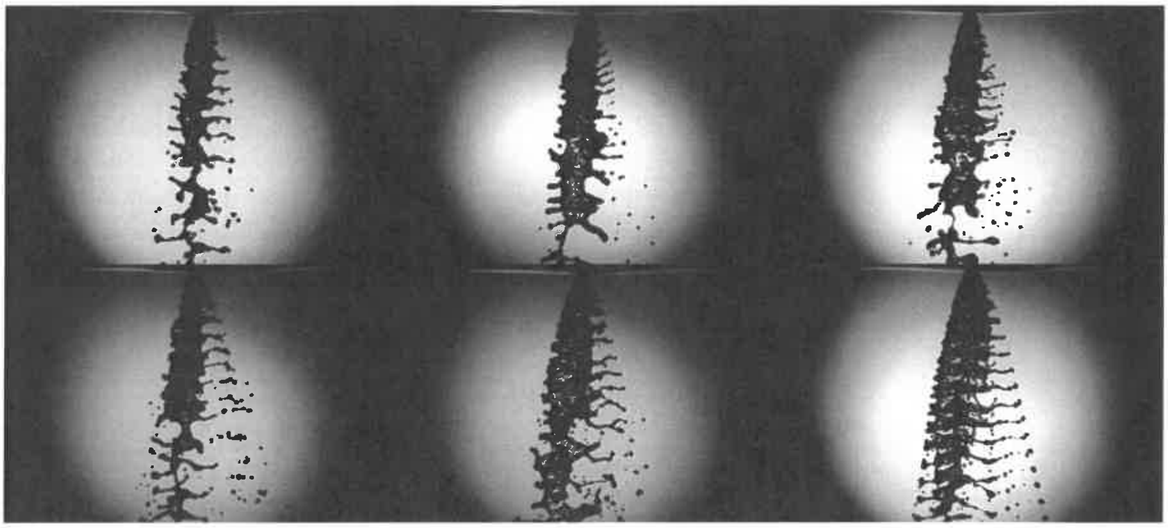

Figure 3

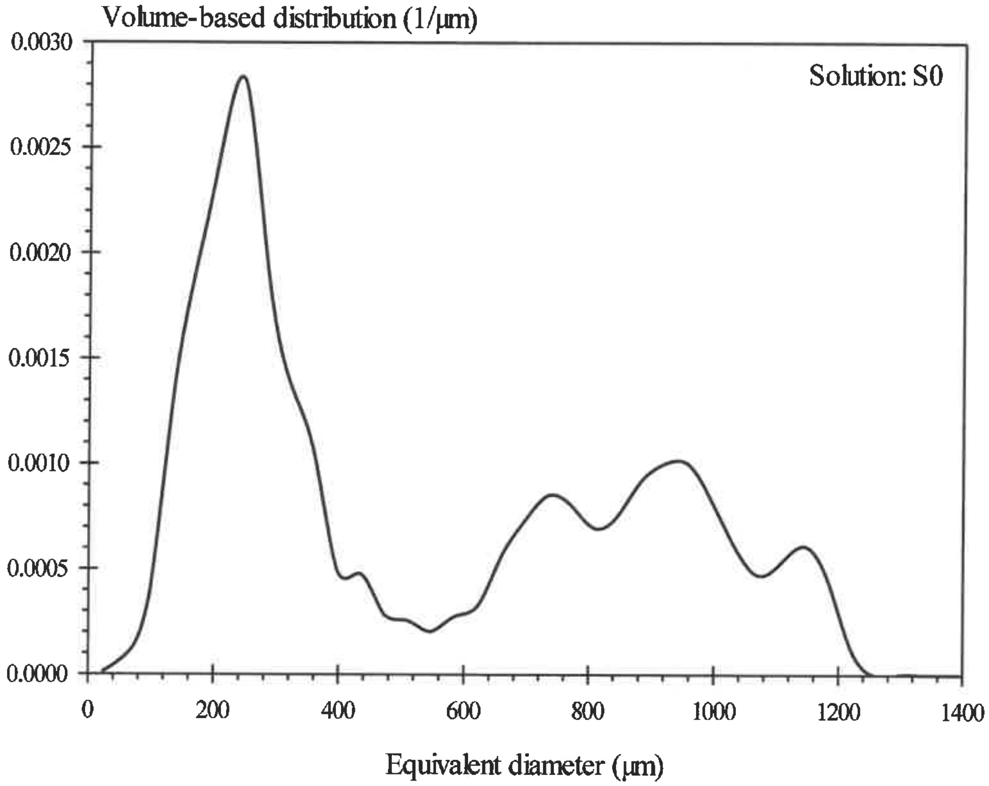

Volume-based distribution (1/µm)
Solution: S0
0.0030
0.0025
0.0020
0.0015
0.0010
0.0005
0.0000
0
200
400
600
800
1000
1200
1400
Equivalent diameter (µm)

Figure 4a

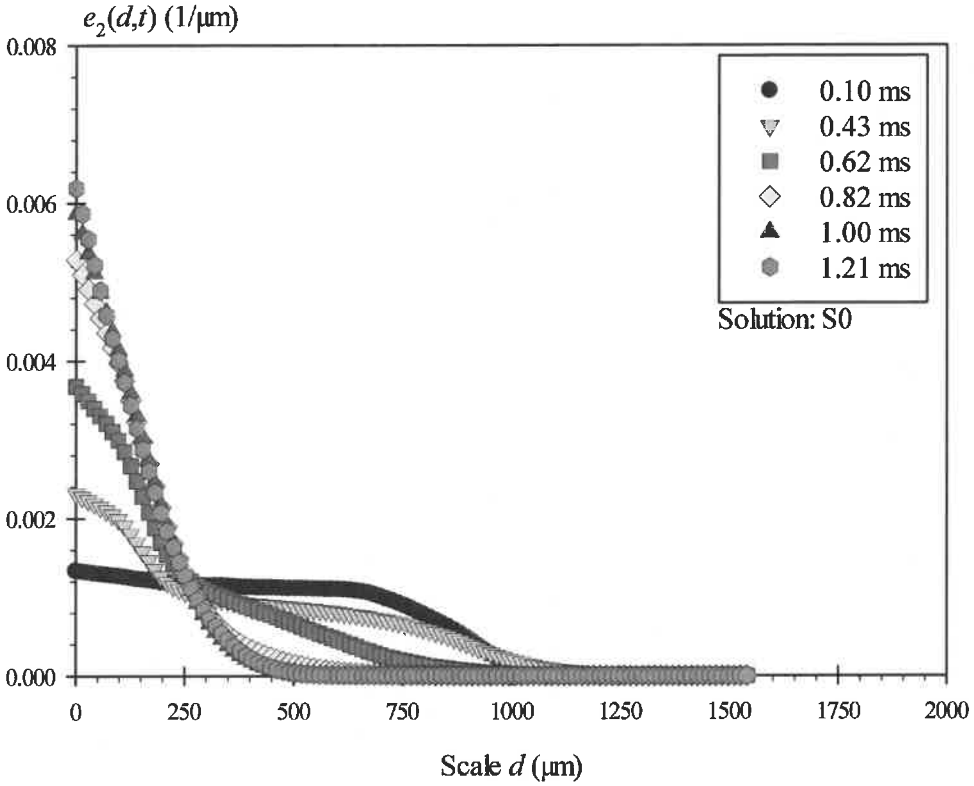
$e_2(d,t)$ (1/μm)
0.008
0.006
0.004
0.002
0.000
0
250
500
750
1000
1250
1500
1750
2000
Scale d (μm)
● 0.10 ms
▽ 0.43 ms
■ 0.62 ms
◇ 0.82 ms
▲ 1.00 ms
⬢ 1.21 ms
Solution: S0

Figure 4b

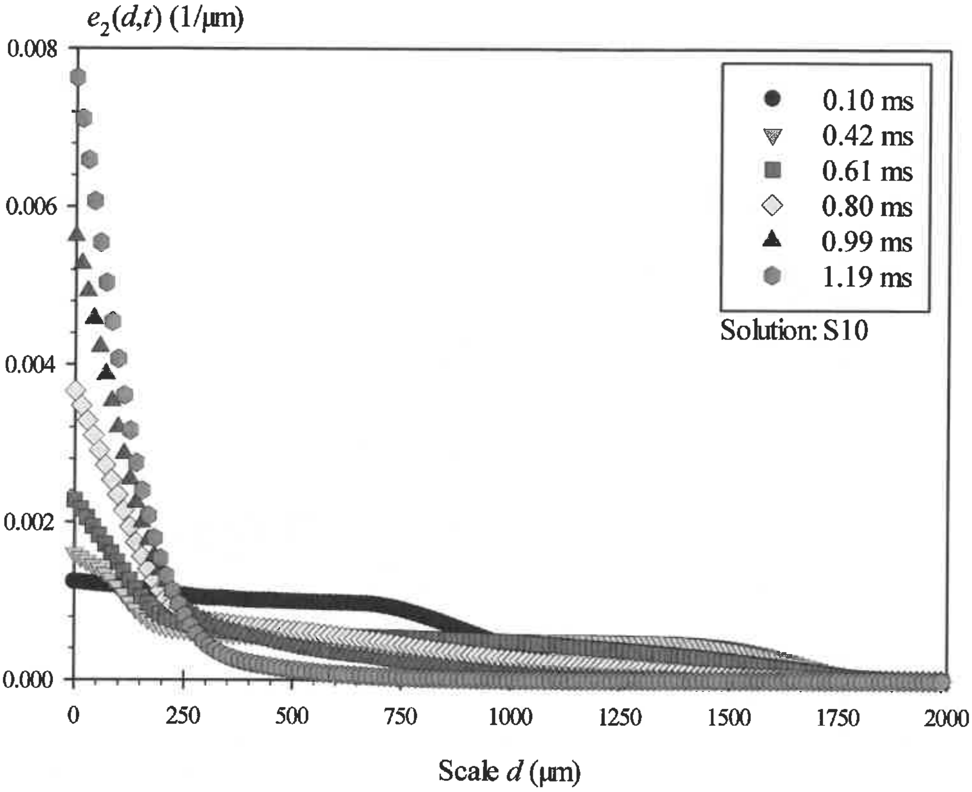
$e_2(d,t)$ (1/µm)
0.008
0.006
0.004
0.002
0.000
0
250
500
750
1000
1250
1500
1750
2000
Scale d (µm)
0.10 ms
0.42 ms
0.61 ms
0.80 ms
0.99 ms
1.19 ms
Solution: S10

Figure 5

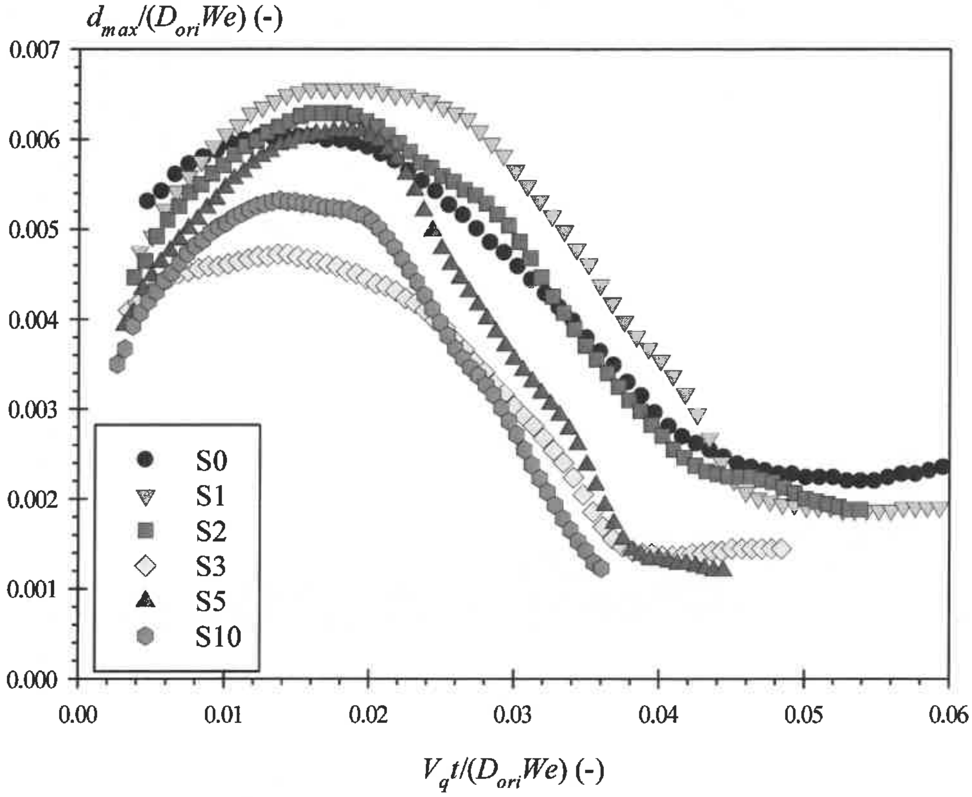
$d_{max}/(D_{ori}We)$ (-)
0.007
0.006
0.005
0.004
0.003
0.002
0.001
0.000
0.00
0.01
0.02
0.03
0.04
0.05
0.06
$V_q t/(D_{ori}We)$ (-)
● S0
▽ S1
■ S2
◇ S3
▲ S5
⬢ S10

Figure 6

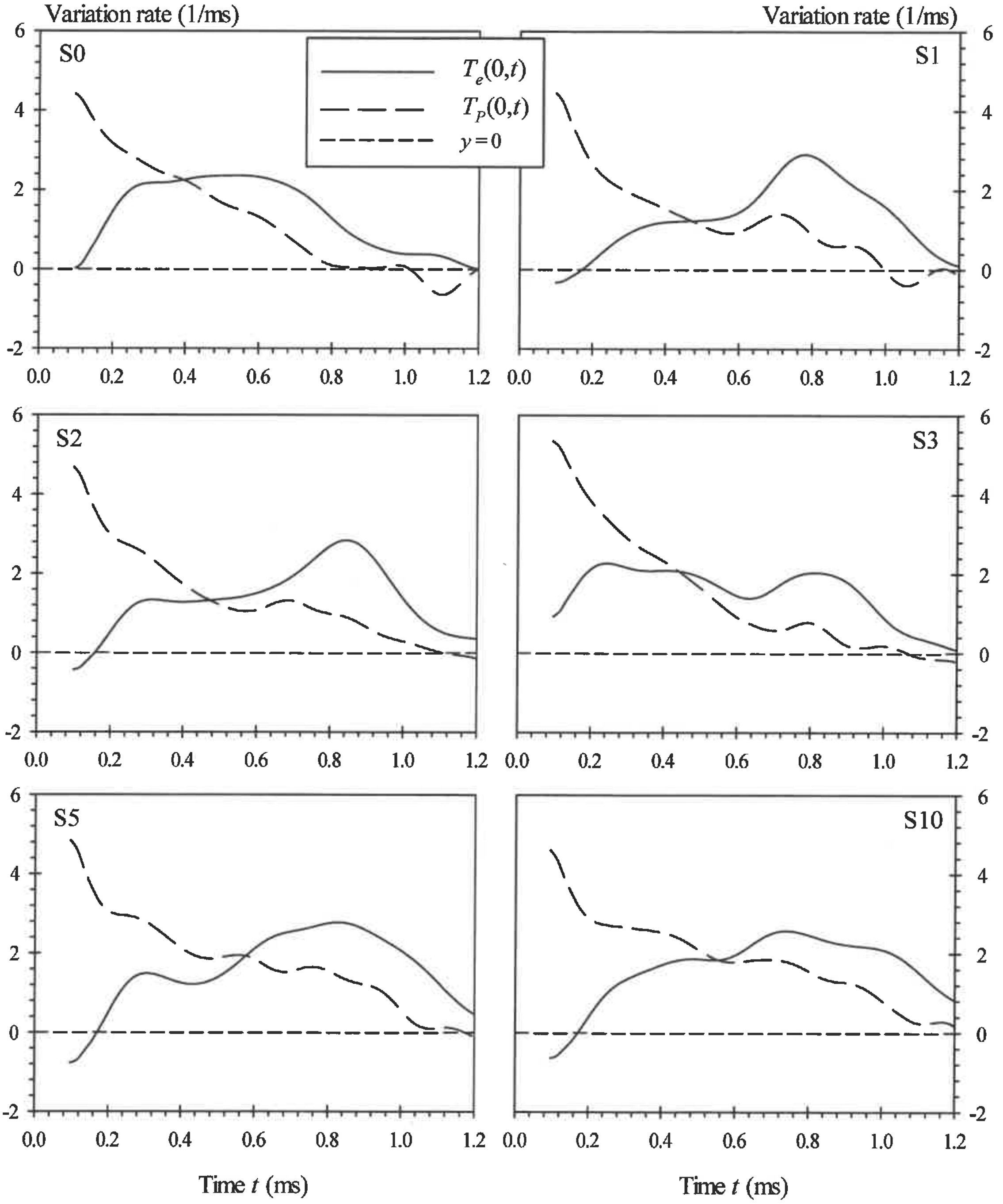
Variation rate (1/ms)
Variation rate (1/ms)
S0
S1
S2
S3
S5
S10
$T_e(0,t)$
$T_P(0,t)$
$y=0$
6
4
2
0
-2
0.0
0.2
0.4
0.6
0.8
1.0
1.2
Time t (ms)
Time t (ms)

Figure 7

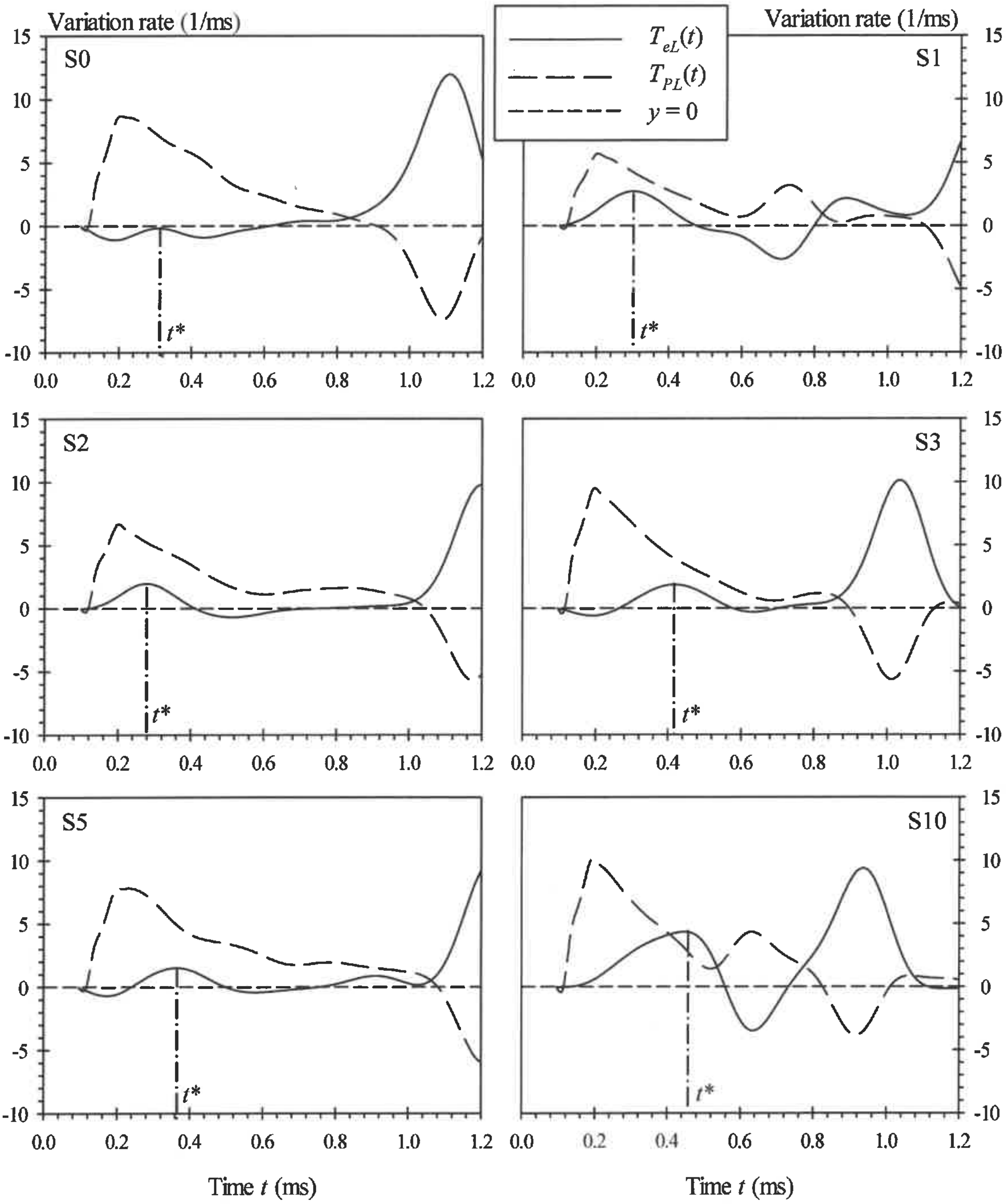
Variation rate (1/ms)
Variation rate (1/ms)
$T_{eL}(t)$
$T_{PL}(t)$
$y = 0$
S0
S1
S2
S3
S5
S10
t^*
15
10
5
0
-5
-10
0.0
0.2
0.4
0.6
0.8
1.0
1.2
Time t (ms)
Time t (ms)

Figure 8

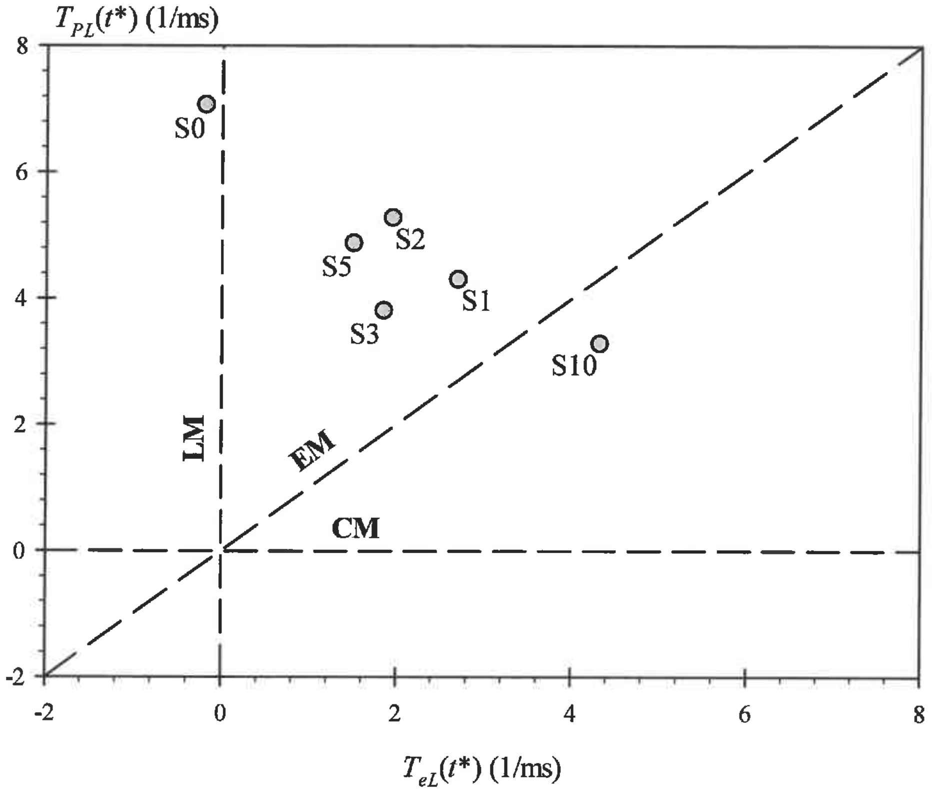

Figure 9

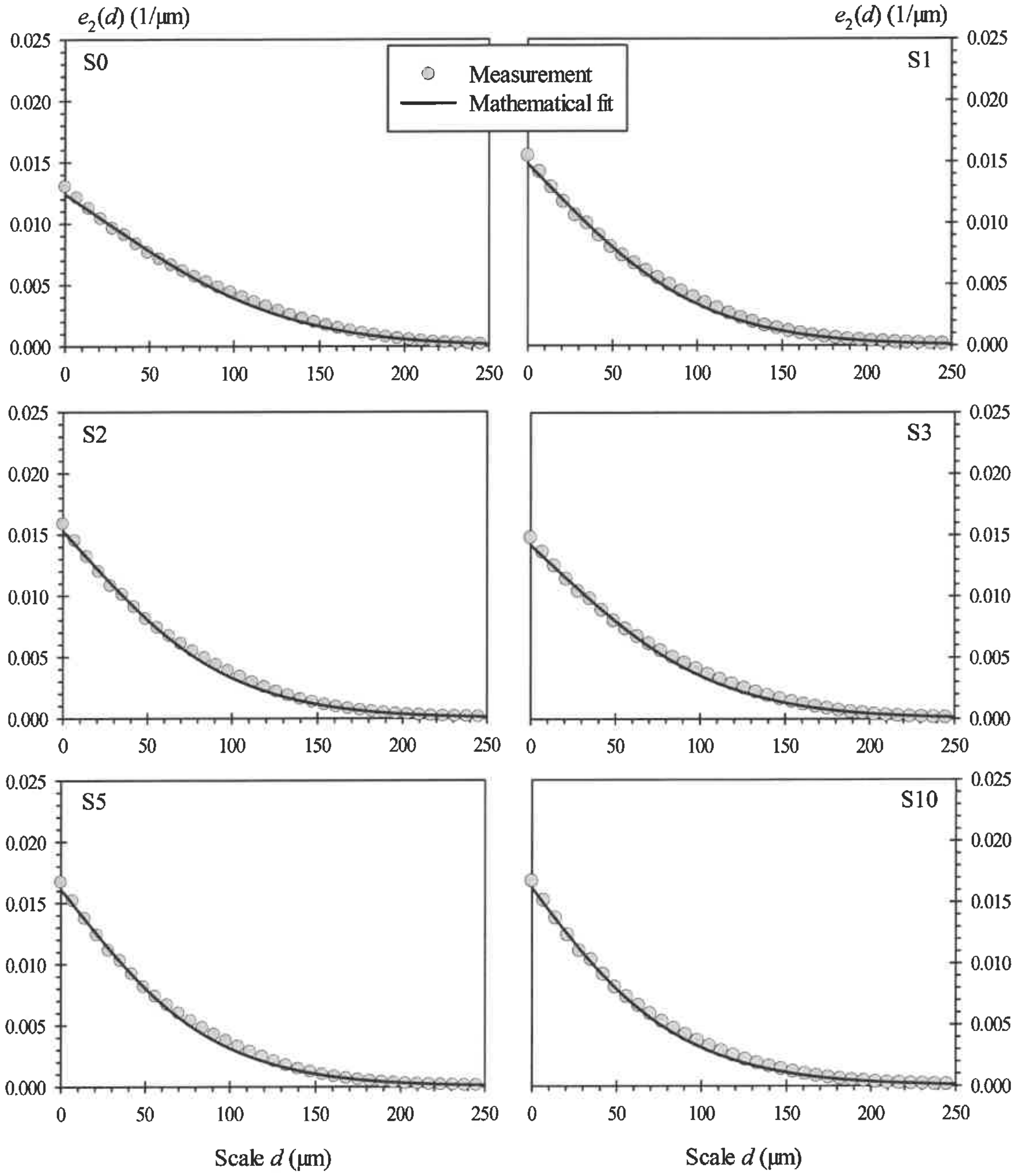
$e_2(d)$ (1/µm)
$e_2(d)$ (1/µm)
0.025
0.020
0.015
0.010
0.005
0.000
S0
S1
S2
S3
S5
S10
Measurement
Mathematical fit
0
50
100
150
200
250
Scale d (µm)
Scale d (µm)

Figure 10

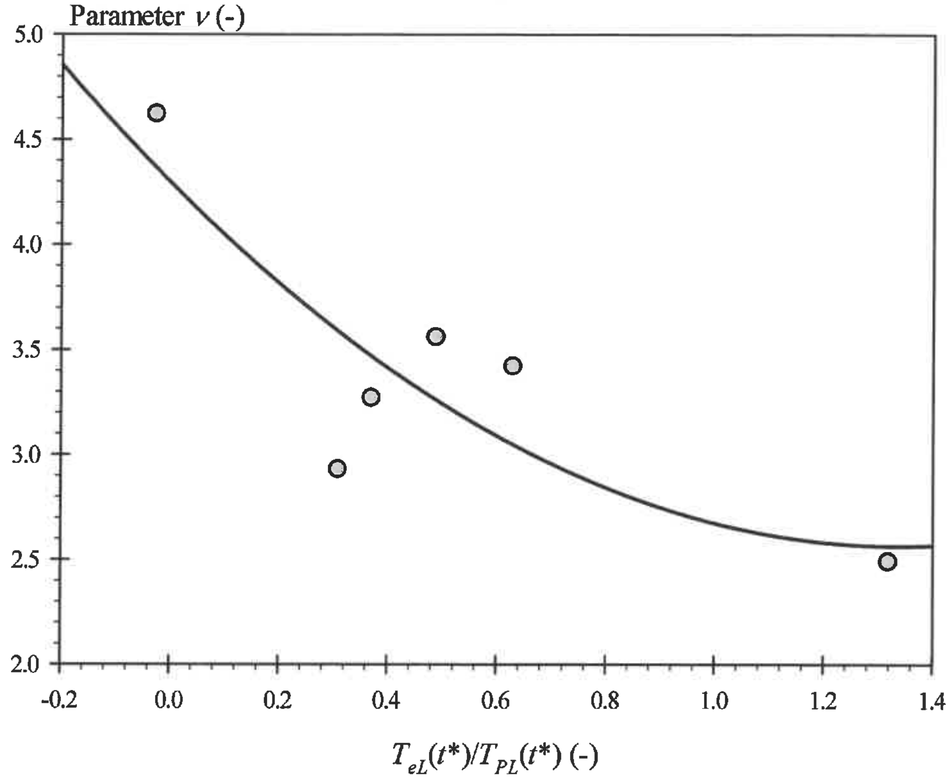
Parameter ν (-)
5.0
4.5
4.0
3.5
3.0
2.5
2.0
-0.2
0.0
0.2
0.4
0.6
0.8
1.0
1.2
1.4
$T_{eL}(t^*)/T_{PL}(t^*)$ (-)

Figure 11

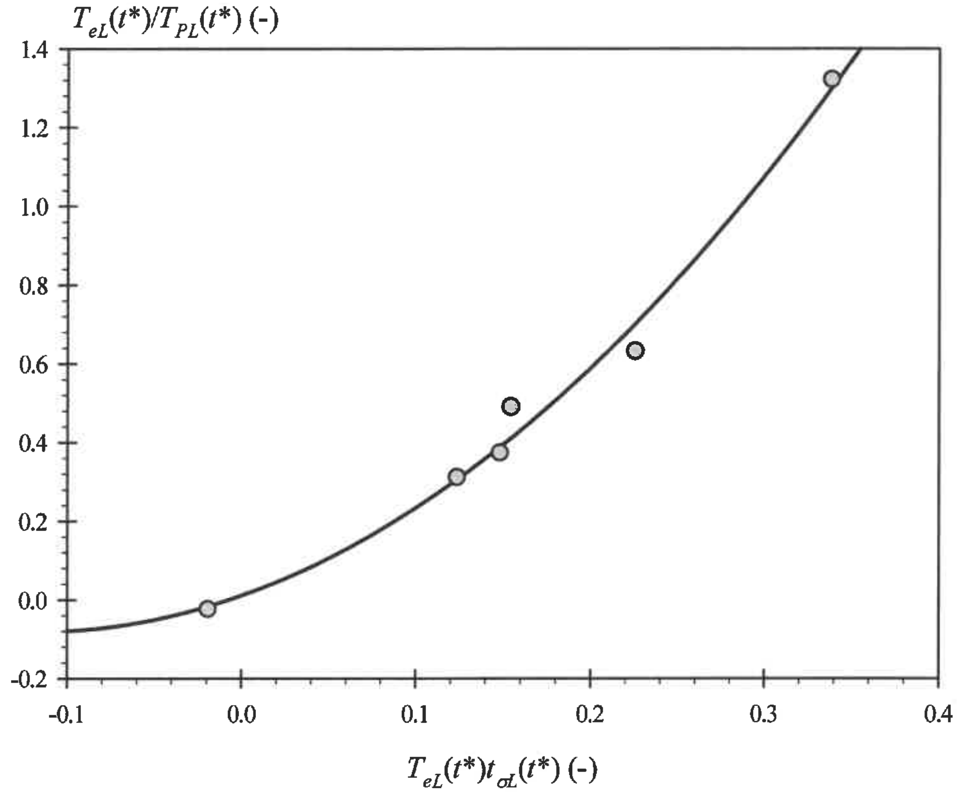

$T_{eL}(t^*)/T_{PL}(t^*)$ (-)
1.4
1.2
1.0
0.8
0.6
0.4
0.2
0.0
-0.2
-0.1
0.0
0.1
0.2
0.3
0.4
$T_{eL}(t^*)t_{\sigma L}(t^*)$ (-)

Figure 12

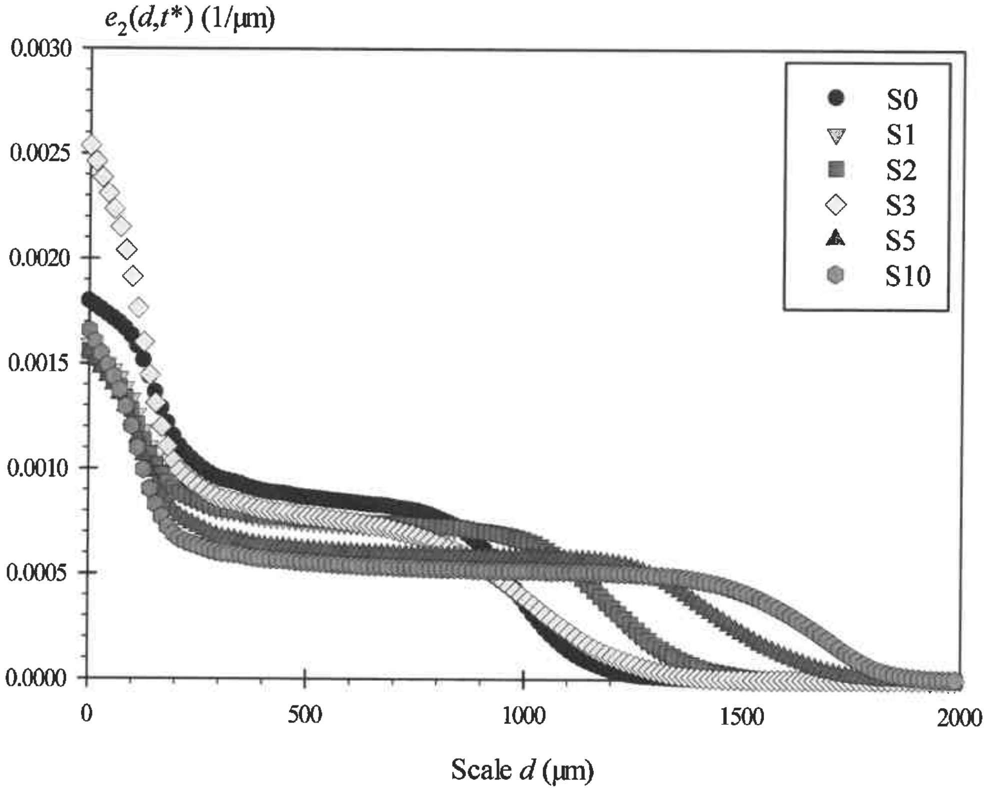
$e_2(d,t^*)$ (1/µm)
0.0030
0.0025
0.0020
0.0015
0.0010
0.0005
0.0000
0
500
1000
1500
2000
Scale d (µm)
● S0
▽ S1
■ S2
◇ S3
▲ S5
● S10

Figure 13

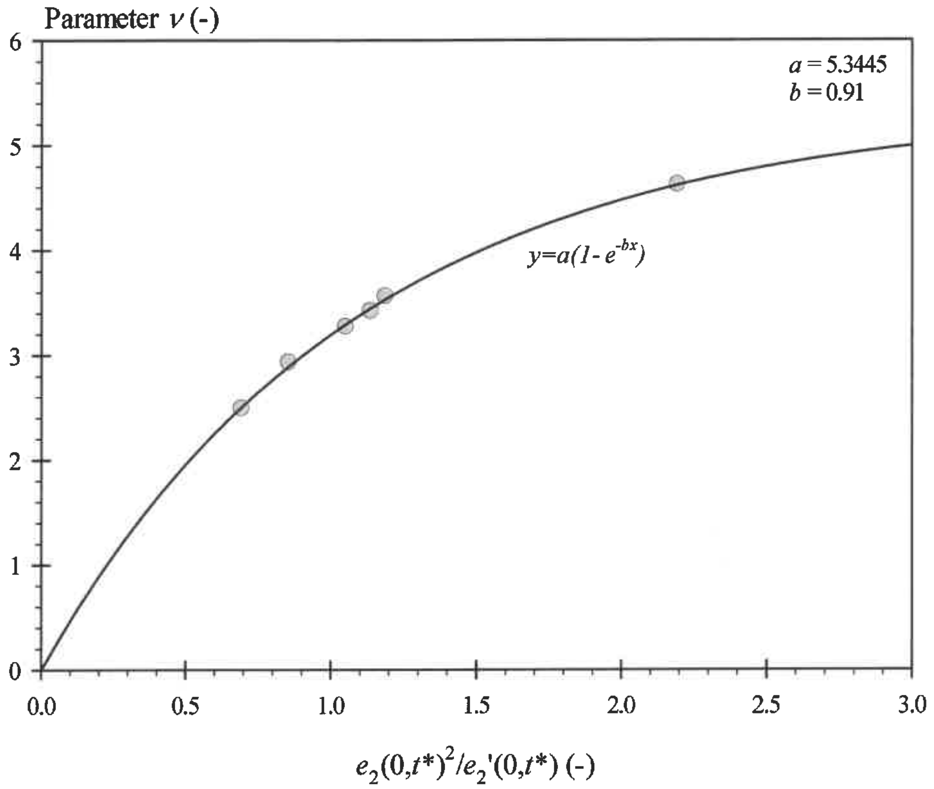
Parameter ν (-)
a = 5.3445
b = 0.91
y=a(1- e^-bx)
0
1
2
3
4
5
6
0.0
0.5
1.0
1.5
2.0
2.5
3.0
e2(0,t*)^2/e2'(0,t*) (-)